American Mineralogist, Volume 81, pages 1222–1236, 1996

Evolution of compositional polarity and zoning in tourmaline during prograde metamorphism of sedimentary rocks in the Swiss Central Alps

RUEDI SPERLICH,[1] RETO GIERÉ,[1,2,*] AND MARTIN FREY[1]

[1]Mineralogisch-Petrographisches Institut der Universität, Bernoullistrasse 30, CH-4056 Basel, Switzerland
[2]Geophysical Laboratory, Carnegie Institution of Washington, 5251 Broad Branch Road NW, Washington, DC 20015, U.S.A.

ABSTRACT

The compositional evolution of tourmaline from diagenetic to lower amphibolite-facies conditions was investigated in two metasedimentary units (redbed and black shale formations) along a traverse across the Central Alps. With increasing metamorphism, three distinct rim zones grew around detrital tourmaline cores, simultaneously with the development of prismatic neoblasts. Detrital cores and all successive rim zones are preserved in the amphibolite-facies rocks. As indicated by whole-rock data, the B required for tourmaline growth was released from illite and muscovite and was not introduced from external sources.

The studied samples of tourmaline exhibit compositional polarity, i.e., their compositions are different at the opposite ends of the *c* axis. The compositional difference between the two poles can be expressed by the substitutions Na + Mg ⇌ □ + Al and 2Al ⇌ Ti + Mg, with the positive pole always richer in Al and having more X-site vacancies. Both chemical and optical polar effects are most pronounced in the internal rim zones and become less prominent toward the external zones. The systematic prograde compositional trends are depicted in a vector space for Li-poor tourmaline. At low-grade conditions, the tourmaline composition is clearly controlled by the host-rock composition, but with increasing metamorphic grade the compositions of tourmaline from a variety of rocks converge. The data show that in the Central Alps, increasing metamorphic grade is reflected by increases in Ca/(Ca + Na) and Mg/(Mg + Fe^{2+}), a decrease in Fe^{3+}, and an increase in the occupancy of the X site of tourmaline.

INTRODUCTION

Tourmaline, a common accessory mineral in clastic metasedimentary rocks, often exhibits authigenic (diagenetic) and metamorphic overgrowths on rounded detrital cores. Authigenic tourmaline exhibits systematic features such as pale colors, a splintery to acicular habit, and polar growth (e.g., Krynine 1946; Mader 1978, 1980). The potential of tourmaline as a petrogenetic indicator in metamorphic rocks was recognized by Frey (1969), and the mineral was subsequently studied in various rock types from different metamorphic grades (e.g., Schreyer et al. 1975; Grew and Sandiford 1984; Henry and Guidotti 1985; Madore and Perreault 1987; Henry and Dutrow 1992). The refractory behavior of tourmaline leads to complex zoning patterns, which are preserved over a wide range of metamorphic conditions and thus offer the possibility to reconstruct the prograde compositional evolution of tourmaline.

In this paper we propose a new vector representation of Li-poor tourmaline and then describe the compositional evolution of tourmaline during prograde metamorphism, from diagenetic to lower amphibolite-facies conditions.

CRYSTAL CHEMISTRY AND VECTOR REPRESENTATION

Tourmaline, $XY_3Z_6(BO_3)_3Si_6O_{18}(O,OH)_3(OH,F)$, shows many possible substitutions between natural and theoretical end-members (Deer et al. 1992). The X site is occupied predominantly by Na and Ca in a ninefold coordination but may also be vacant. The Y and Z sites are both octahedrally coordinated; divalent cations are incorporated preferentially into the Y site, whereas Al^{3+} generally enters the smaller Z site. Detailed surveys on structure, crystal chemistry, and substitutions were given by, e.g., Povondra (1981), Burt (1989), Henry and Dutrow (1990), and Grice and Ercit (1993).

Because the X, Y, and Z sites can be occupied by a variety of cations, the chemical variability of tourmaline is extensive. A convenient way of representing such compositional variations is by the use of exchange vectors that delineate the compositional space of interest (Thompson 1982). This method was adapted to the tourmaline-group minerals by Burt (1989). A clear vector rep-

*Author to whom all correspondence should be addressed. Address for correspondence: Mineralogisch-Petrographisches Institut der Universität, Bernoullistrasse 30, CH-4056 Basel, Switzerland.

0003–004X/96/0910–1222$05.00

TABLE 1. Main independent substitutions and corresponding end-members in Li-poor tourmaline

Substitutions*	Exchange vectors	End-members
$^{Y}Mg = {}^{Y}Fe^{2+}$	$Fe^{2+}Mg_{-1}$	schorl, $NaFe^{2+}_3Al_6(BO_3)_3Si_6O_{18}(OH)_4$
$^{X}Na + {}^{Z}Al = {}^{X}Ca + {}^{Z}Mg$	$CaMgNa_{-1}Al_{-1}$	uvite, $CaMg_3(MgAl_5)(BO_3)_3Si_6O_{18}(OH)_4$
$^{X}Na + {}^{Y}Mg = {}^{X}\square + {}^{Y}Al$	$\square AlNa_{-1}Mg_{-1}$	alkali-free tourmaline, $^{X}\square(Mg_2Al)Al_6(BO_3)_3Si_6O_{16}(OH)_4$
$^{Y}Mg + (OH) = {}^{Y}Al + O$	$AlOMg_{-1}(OH)_{-1}$	olenite, $NaAl_3Al_6(BO_3)_3Si_6O_{16}(O_3OH)$

* Substitutions starting from dravite: $NaMg_3Al_6(BO_3)_3Si_6O_{18}(OH)_4$. Superscripts represent structural sites. $^{X}\square$ = vacancy on X site.

resentation of tourmaline, however, is not possible without some simplifications because the mineral commonly contains more than ten important chemical constituents.

A first step in reducing the number of components consists in disregarding the Li end-members elbaite and liddicoatite. This assumption is justified because tourmaline occurring in schists is typically very low in Li (Foit and Rosenberg 1977; Dutrow et al. 1986; Grew et al. 1990). Moreover, Li-rich tourmaline is mainly found in Li-rich granitoid pegmatites and aplites (Henry and Guidotti 1985).

To start, we consider only the Fe^{2+} content because the concentration of Fe^{3+} strongly depends on the redox conditions prevailing in the different rock types (see below). Moreover, we ignore the small quantities of K, Mn, Cr, Ti, and F and also do not allow for variation in B (usually stoichiometric) and Si (Al generally does not substitute for Si; see, e.g., Deer et al. 1992). The number of components, thus, has been reduced to six: Na, Ca, Fe^{2+}, Mg, Al, and $^{X}\square$ (X-site vacancy). Assuming further that no elements other than Na and Ca occupy the X site, the four most important independent substitutions for tourmaline in schists can be formulated as follows:

$$^{Y}Mg = {}^{Y}Fe^{2+} \quad (1)$$

$$^{X}Na + {}^{Z}Al = {}^{X}Ca + {}^{Z}Mg \quad (2)$$

$$^{X}Na + {}^{Y}Mg = {}^{X}\square + {}^{Y}Al \quad (3)$$

$$^{Y}Mg + (OH) = {}^{Y}Al + O. \quad (4)$$

Alternatively, these substitutions can be expressed as exchange vectors. Taking dravite as the additive component, application of the exchange vectors leads to the four end-members schorl, uvite, alkali-free tourmaline, and olenite (Table 1). The number of independent exchange vectors can be reduced to three by introducing the new variable M, defined as $M = Fe^{2+} + Mg$ (molar quantities).

Because these three substitutions all lead to a change in M, and because Substitution 4 additionally involves components not readily analyzed by electron microprobe, it is generally difficult to determine the proportions of each end-member in a given tourmaline. To overcome this problem, we propose a vector representation that departs in some aspects from that of, e.g., Burt (1989) and Henry and Dutrow (1990). Our representation is based on the following observation: The variation in M described by Substitutions 2 and 3 is associated with a change in X-site components; the variation in M resulting from Substitution 4, however, is independent of the X-site components. Therefore, we introduce two new variables, M_x and M_{ol}, to account for the two mechanisms; these variables are related to each other by the equation

$$M = M_x + M_{ol}. \quad (5)$$

Figure 1A shows a triangular vector prism where the basal plane is defined by the vectors $CaM_xNa_{-1}Al_{-1}$ and $\square AlNa_{-1}(M_x)_{-1}$ with dravite-schorl as the starting point

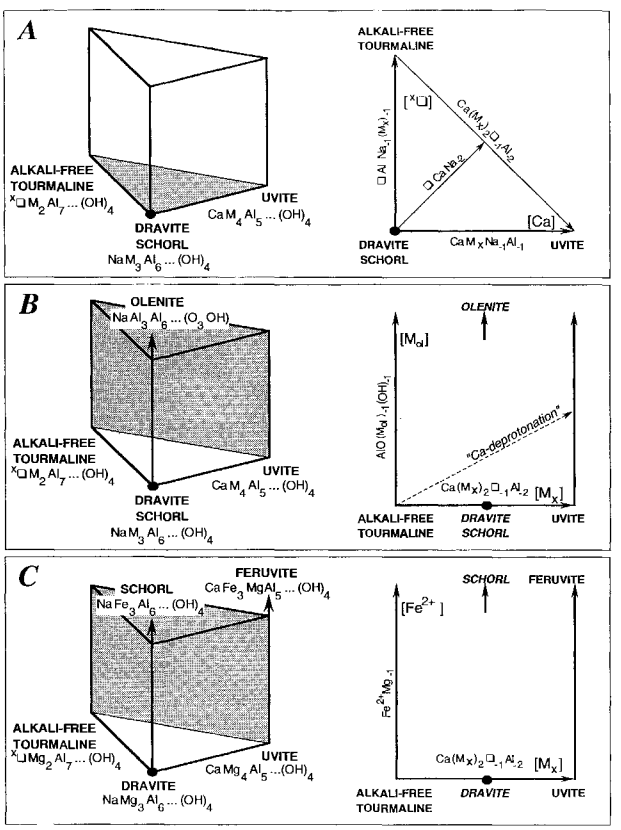

FIGURE 1. Compositional prisms for Li-poor tourmaline, generated by the basic exchange vectors listed in Table 1. (**A**) Basal plane showing the system alkali-free tourmaline, dravite-schorl, and uvite; (**B**) back face showing the system alkali-free tourmaline, uvite, dravite-schorl, and olenite; (**C**) back face showing the system alkali-free tourmaline, uvite, feruvite, dravite, and schorl. Shaded prism faces are shown on the right as diagrams with the appropriate substitutions. Plot components are given in square brackets. End-members written in italics represent perpendicular projections onto the shaded prism face.

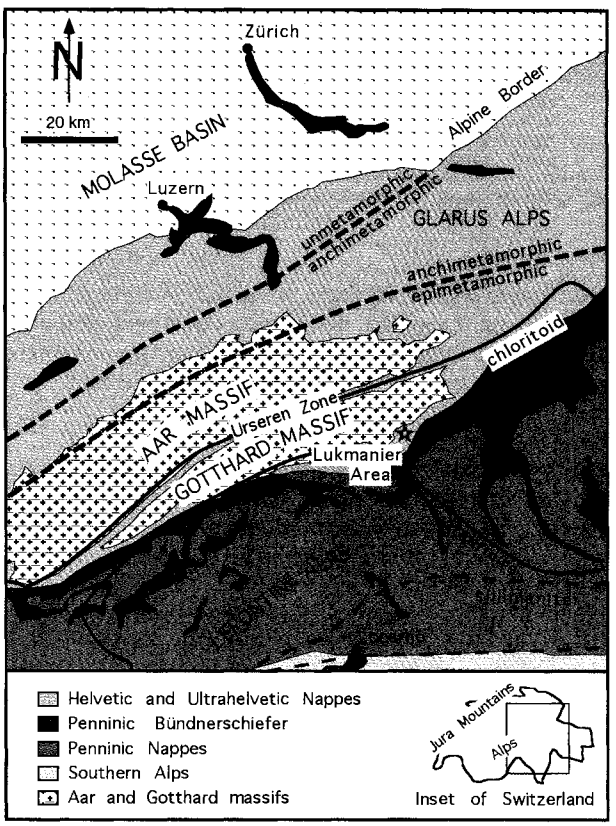

FIGURE 2. Simplified tectonic map of the Central Alps. Alpine metamorphic conditions are indicated by mineral-zone boundaries for chloritoid-in, staurolite-in, and sillimanite-in. The chloritoid-in and staurolite-in mineral-zone boundaries represent approximately the transitions from stage I to stage II and from stage II to stage III of tourmaline growth, respectively. Star symbol marks the Val Cavalasca locality (see Fig. 13).

(cf. Henry and Dutrow 1990). Tourmaline data lying in the basal plane can be displayed by plotting the amount of Ca and $^{X}\square$. The value of M_x increases from alkali-free tourmaline (M_x = 2.0) to uvite (M_x = 4.0) along $Ca(M_x)_2\square_{-1}Al_{-2}$, a vector representing a linear combination of $CaM_xNa_{-1}Al_{-1}$ and $\square AlNa_{-1}(M_x)_{-1}$. Figure 1A reveals that the value of M_x can be calculated from the equation

$$M_x = 2.0 + Na + 2Ca \quad (6)$$

and that lines of constant M_x are perpendicular to $Ca(M_x)_2\square_{-1}Al_{-2}$, i.e., parallel to $\square CaNa_{-2}$.

Now, we additionally consider the exchange vector that is independent of the X-site components. This vector, $AlO(M_{ol})_{-1}(OH)_{-1}$, leads toward the olenite end-member and is chosen to be perpendicular to the basal plane of the prism (Fig. 1B). To determine the extent of the olenite substitution, we project the data along $\square CaNa_{-2}$ onto the back face of the prism; this projection does not affect the values of M_x and Al. From Figure 1B it is evident that the back face of the prism is defined by $Ca(M_x)_2\square_{-1}Al_{-2}$ and $AlO(M_{ol})_{-1}(OH)_{-1}$. This plane can therefore be used to display the extent of olenite substitution in tourmaline. M_{ol} can be calculated from Equations 5 and 6 and is given by

$$M_{ol} = M - 2.0 - Na - 2Ca$$
$$= Fe^{2+} + Mg - 2.0 - Na - 2Ca. \quad (7)$$

Because the olenite substitution leads to a decrease in total M, the value of M_{ol} is a negative number. Henry and Dutrow (1990) argued that Ca is incorporated into aluminous tourmaline mainly by "Ca-deprotonation" (see Fig. 1B). This vector, $CaMgO\square_{-1}Al_{-1}(OH)_{-1}$, however, can be described as a linear combination of $CaM_xNa_{-1}Al_{-1}$, $\square AlNa_{-1}(M_x)_{-1}$, and $AlO(M_{ol})_{-1}(OH)_{-1}$ (Burt 1989).

So far, we have not considered Substitution 1. We can evaluate the extent of this substitution by using a compositional space defined by the basal plane of the prism and the $Fe^{2+}Mg_{-1}$ exchange vector, which allows for representation of schorl and feruvite (Grice and Robinson 1989). Figure 1C shows that the projection onto the back face of the prism offers the possibility to compare the $Fe^{2+}Mg_{-1}$ exchange with the coupled Substitutions 2 and 3 and, thus, to determine whether these substitutions preferentially involve Mg or Fe^{2+}.

An advantage of the proposed vector representation of Li-poor tourmaline is that a simple graphical display can be used to evaluate the extent of the olenite substitution, which is difficult to assess by other means. Furthermore, the importance of Fe can be compared with multisite coupled substitutions (e.g., incorporation of Ca) in a single graph. Our vector representation is used to display compositional trends observed for tourmaline from the Swiss Central Alps.

GEOLOGIC SETTING

The tourmaline crystals occur in well-studied rocks that underwent a single metamorphic event. The geologic traverse follows Upper Triassic (Keuper) redbeds, known as Quartenschiefer, and Lower Jurassic (Lias) black shales between the Jura mountains and the Lukmanier area in the Central Alps (Fig. 2). The redbed series comprises graphite-free pelites, marls, sandstones, and dolomites, whereas the black shales consist of pelites, marls, sandstones, and arenaceous limestones containing organic material. The metamorphic grade of these rocks increases from the Jura mountains (unmetamorphosed) to the anchimetamorphic Glarus Alps (200–300 °C, 2–3 kbar), then to lower greenschist facies in the Urseren Zone, and finally to upper greenschist and lower amphibolite facies (500–550 °C, 5–7 kbar) in the Lukmanier area (see Fig. 2; Frey 1969, 1974, 1978; Fox 1975; Engi et al. 1995).

ANALYTICAL CONDITIONS

Tourmaline was analyzed by a wavelength-dispersive electron microprobe (JEOL JXA 8600) operated at 15 kV and with a sample current of 20 nA. Ten elements were sought using well-characterized minerals and synthetic

compounds as standards. Data from all detected elements were fully corrected for ZAF matrix effects. To detect the complete zoning patterns of tourmaline, we studied the crystals by backscattered electron imaging prior to selecting suitable locations for quantitative analysis. Utmost care was taken to avoid mixed analyses resulting from contamination by X-ray emission from adjacent zones at chemical discontinuities such as zone or grain boundaries.

Petrographic features and optical zoning

Tourmaline is a refractory mineral, i.e., it exhibits very slow intracrystalline or volume diffusion and therefore preserves its zoning patterns during prograde metamorphism (e.g., Dietrich 1985). In the studied geologic traverse we observed the following features:

Diagenesis to lower greenschist facies (stage I)

In the unmetamorphosed sedimentary rocks, tourmaline occurs as rounded detrital grains with authigenic rims. The latter exhibit some typical features, which are independent of size, shape, and composition of the detrital cores and which are not controlled by the mineral content of the rocks: The rims are always anhedral, with a splintery to acicular shape and a dentate boundary, and almost exclusively grew in one direction away from the detrital core (Fig. 3A). Previous studies have shown that such overgrowths develop preferentially at the positive pole of the crystallographic *c* axis of the cores (e.g., Alty 1933; Awashti 1961). Syntaxy between core and rim is indicated by the continuity of optical properties (e.g., extinction across the core-rim boundary). Generally, the color of the overgrowths varies considerably (see below), but its variation is not systematically and significantly different in the different rock types. The diagenetic rims are rich in inclusions of quartz but also contain rutile, apatite, and graphite (in black shales only) and in some cases have replaced illite-muscovite and chlorite (Fig. 3B). Similar observations were recently reported by Henry and Dutrow (1992). The diagenetic rims do not disappear with increasing metamorphic grade. Moreover, tourmaline inclusions in chloritoid exhibit rims of stage I only, implying that the rims of stage II (see below) do not start growing until middle greenschist-facies conditions are reached (at 400–450 °C in the studied area). From these observations it follows that the rims of stage I do not necessarily represent diagenetic overgrowths only, but that they could have continued to grow during the later prograde metamorphism. This is also indicated by the continuous zoning with respect to the concentration of Fe and Mg during stage I (see below).

Middle to upper greenschist facies (stage II)

The rims of stage I are separated from the first clearly metamorphic rims (stage II) by a sharp boundary with a discontinuous change in both color and composition. In contrast to the strongly asymmetric diagenetic rims, the growth of tourmaline during stage II seems to have taken place in both directions of the *c* axis (Fig. 3C). These metamorphic overgrowths are subhedral to euhedral in shape, disrupted only by large grains of quartz, calcite, or dolomite. Other inclusions observed are rutile, ilmenite, apatite, and graphite (in black shales only), but they are significantly less abundant than in the rims of stage I. Stage II is not only characterized by the formation of euhedral rims around older tourmaline crystals but also by the appearance of new, needle-shaped and coreless tourmaline crystals. The latter are disseminated throughout the rock without recognizable textural relationship to the larger zoned tourmaline crystals; it appears, thus, that these needles have nucleated independently. The metamorphic rims of stage II are generally green in metapelites, but yellow and brown in marls and carbonate-rich rocks; the colors are always more intense than those exhibited by the diagenetic rims. Tourmaline grains with rims of stage II commonly appear as inclusions in biotite, garnet, and kyanite, and occasionally in staurolite.

Amphibolite facies (stage III)

The second generation of metamorphic rims appears slightly above the staurolite-in mineral-zone boundary, i.e., approximately at the upper end of the chloritoid zone in the Lukmanier area (Fig. 2). These tourmaline rims (stage III), like those of stage II, are often characterized by a large volume. They are generally euhedral, particularly in mica-rich layers, and contain only a few inclusions. Usually, the rims of stage III are optically homogeneous, but occasionally they exhibit two subzones. There is only a slight difference in color between the rims of stages II and III, but the boundary between these two overgrowths is always discontinuous and clearly visible (Fig. 3C).

It is noteworthy that strongly zoned tourmaline was found also in other metasedimentary units within the staurolite zone of the Central Alps (Thakur 1972; Gieré and Rumble 1994a, 1994b) and at several other localities in high-grade metamorphic terrains (e.g., Smith 1971; Grew and Sandiford 1984; Henry and Guidotti 1985; Dutrow and Henry 1994). We stress that in all these cases, the orientation of tourmaline sections is crucial for investigating the growth history. If sections perpendicular to the *c* axis are used exclusively, the probability of obtaining sections across the nearly homogeneous rims of stage III is very high (Fig. 4, section A). Moreover, cross sections of internal parts of the crystal may display complex zoning patterns resulting from the dentate boundary between the rims of stages I and II (Fig. 4, sections B and D); the complex geometry exhibited by such sections often does not allow ready interpretation of the zoning with regard to the growth history of tourmaline unless longitudinal sections are studied as well. If various types of zoning patterns are observed in different cross sections of a single sample, the sample does not necessarily contain different types of tourmaline. Therefore, it is necessary to use at least one longitudinal section to detect the complete zoning record in tourmaline.

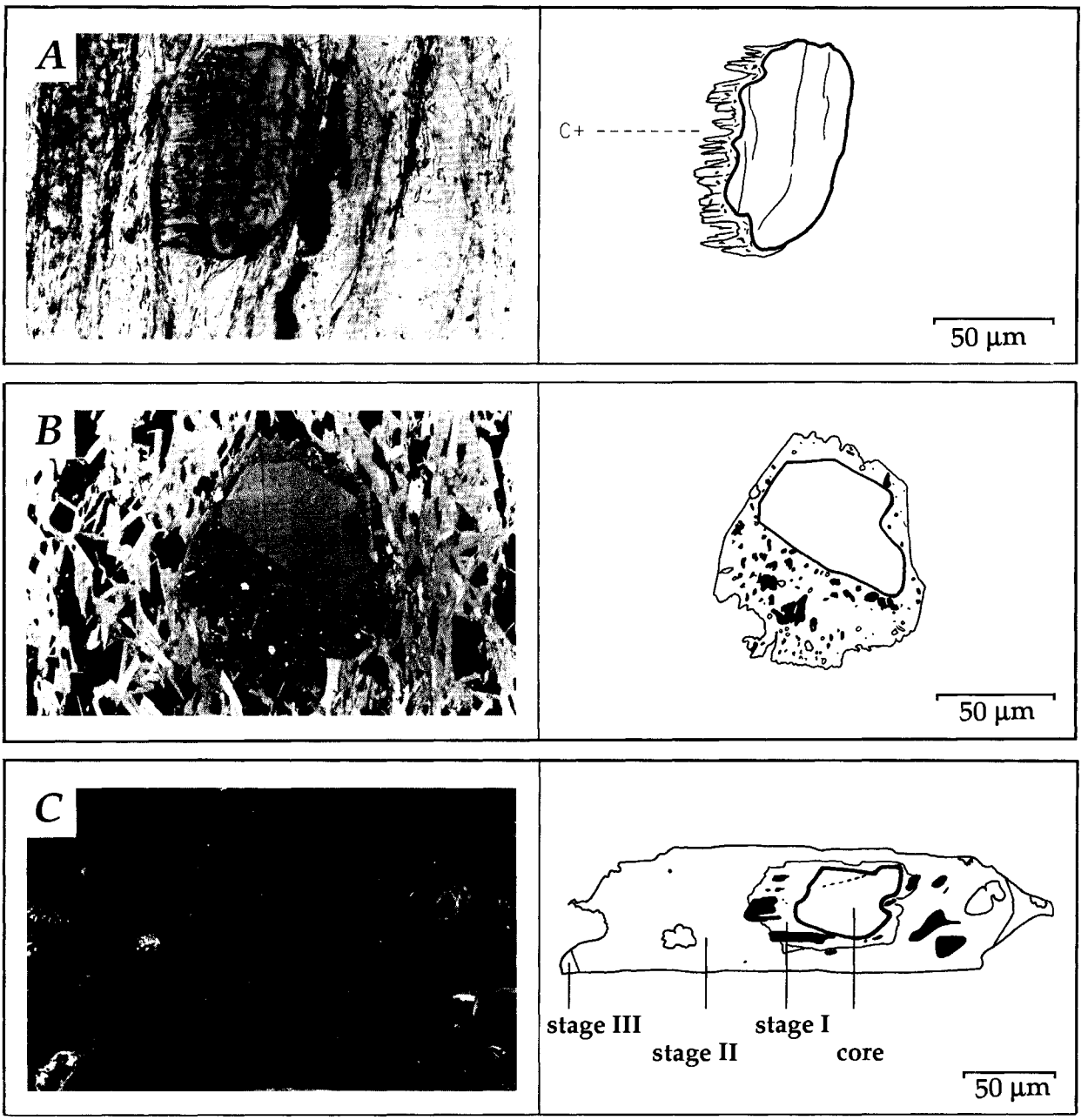

FIGURE 3. (A) Photomicrograph showing low-grade (stage I) overgrowth on a detrital tourmaline grain. Note the preferred growth toward the positive pole of the *c* axis (sample MF 134). (B) Backscattered electron (BSE) image of a low-grade tourmaline. The replacement of white mica (gray) and chlorite (white) results in abundant relic quartz inclusions (black) within the tourmaline rim. The *c* axis is not parallel to the plane of the photograph (sample MF 330). (C) BSE image of a staurolite-zone tourmaline at the beginning of stage III. Detrital core and all rim generations from diagenesis to amphibolite facies are preserved. The larger parts to the left correspond to the positive *c* axis. Note the abundant quartz inclusions (black) within the internal rim (sample MF 1632).

COMPOSITIONAL POLARITY

Tourmaline is known for its polar physical properties (e.g., hemimorphism, piezoelectricity, and pyroelectricity). These can be explained crystallographically by the orientation of the SiO_2 tetrahedra, which point toward the negative end of the *c* axis (*c*−; Barton 1969). Morphologically, the polarity is expressed by the steeper basal pyramids at the positive end of the *c* axis (*c*+; see Fig. 4). A pronounced effect of polarity is the preferred growth of diagenetic rims on *c*+ of detrital tourmaline cores in

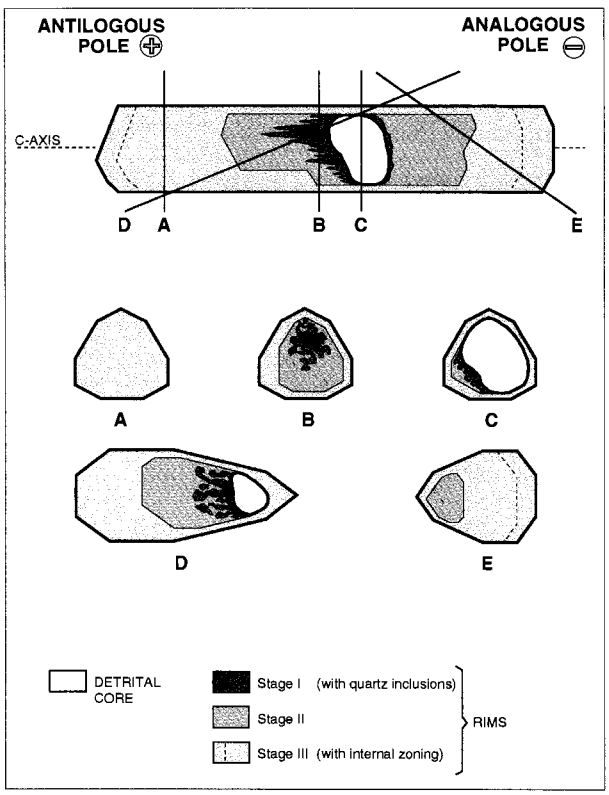

FIGURE 4. Schematic longitudinal section through a representative amphibolite-facies tourmaline with the typically large volume of stage III. Randomly oriented sections (**A–E**) are shown to demonstrate how they can lead to confusing zoning patterns because critical information is missing.

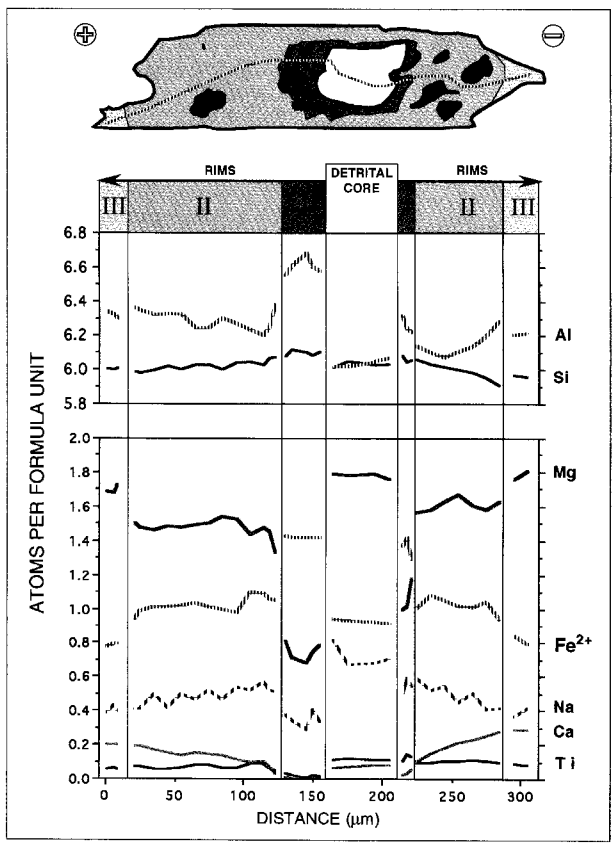

FIGURE 5. Longitudinal profile through the amphibolite-facies tourmaline shown in Figure 3C (sample MF 1632; Lias black shale), illustrating compositional polarity and discontinuous transitions among different rim zones. Quartz inclusions are shown in black.

sedimentary rocks. Generally, the positive part of the overgrowth is longer at later growth stages as well (Henry and Dutrow 1992).

Another aspect of the polar properties of tourmaline is the existence of compositional polarity, i.e., difference in composition between $c+$ and $c-$ of a crystal. This observation was first reported by Sperlich (1990) and later by Henry and Dutrow (1992). The effects of compositional polarity may be recognized in thin section as differences in color: In the studied rock sequences from the Central Alps, the positive part of the innermost rim (stage I) is colorless to pale blue or bluish green, whereas the corresponding negative part, on the other side of the detrital core, is yellow to reddish brown. The colors of the rims of stages II and III, however, are very similar at both ends, suggesting that the compositional polarity is less pronounced.

Characteristic color differences are probably, at least in part, the result of a variation in Ti content (Lowell and Vierrether 1989; Slack and Coad 1989). To correlate the chemical composition with the optically visible zoning and color patterns, a series of electron microprobe analyses was obtained along a traverse through a tourmaline crystal with the described characteristic zoning features. The selected crystal, typical for the onset of stage III (Fig. 3C), occurs in staurolite-grade black shales south of Lukmanier pass (Fig. 2; Swiss coordinates: 697.025/155.700). The host rock contains abundant staurolite, quartz, muscovite, margarite, graphite, and garnet (with many inclusions of chloritoid), as well as lesser amounts of plagioclase, biotite, and ilmenite (sample MF1632). The chemical profiles through the selected crystal (Fig. 5) demonstrate that the rims of all three growth stages are separated from each other by marked chemical discontinuities, which coincide spatially with the optically visible boundaries. Figure 5 further shows that the chemical composition of tourmaline varies continuously across individual rims. Moreover, this crystal documents very clearly the existence of compositional polarity. The difference in composition between the $c+$ and $c-$ poles is most pronounced at the outer margin of the rim grown during stage I, and becomes less marked toward the external rims. This is demonstrated in particular by the contents of Al, Mg, and Na, as well as by the number of $^{X}\square$ (Table 2). The concentrations of most other components are also different at $c+$ and $c-$, and these differ-

TABLE 2. Compositional polarity between positive ($c+$) and corresponding negative ($c-$) poles for tourmaline rims grown during stages I–III

	Stage I		Stage II		Stage III	
	Δx_i	2σ	Δx_i	2σ	Δx_i	2σ
			Inner margin			
Si	0.024	0.035	0.012	0.034	0.040	0.034
Al	0.262	0.027	0.242	0.027	0.094	0.027
Ti	−0.088	0.005	−0.051	0.005	−0.036	0.006
Fe	0.042	0.018	0.047	0.016	−0.047	0.018
Mg	−0.213	0.016	−0.227	0.021	−0.032	0.022
Ca	−0.016	0.003	−0.066	0.004	−0.086	0.007
Na	−0.158	0.014	−0.081	0.016	0.028	0.015
K	0.002	0.001	0.002	0.001	−0.002	0.002
X-site vacancies	0.172	0.014	0.145	0.017	0.060	0.016
			Outer margin			
Si	0.026	0.034	0.078	0.034	0.051	0.034
Al	0.335	0.027	0.079	0.027	0.123	0.027
Ti	−0.096	0.005	−0.029	0.006	−0.022	0.005
Fe	0.134*	0.018	−0.001	0.014	−0.015	0.017
Mg	−0.364	0.018	−0.130	0.022	−0.121	0.022
Ca	−0.046	0.004	−0.085	0.007	−0.092	0.007
Na	−0.172	0.016	−0.007	0.013	−0.026	0.013
K	—	—	—	—	−0.002	0.002
X-site vacancies	0.218	0.016	0.092	0.015	0.120	0.015

Note: All data from sample MF1632 (Lias black shale, amphibolite facies). Magnitude of compositional polarity is given as Δx_i, defined as $\Delta x_i = x_i(c+) - x_i(c-)$ for inner and outer margins of individual rims (as atoms per formula unit, on the basis of 24.5 O atoms). Uncertainty of Δx_i, resulting from counting statistics of electron microprobe analyses, is listed as 2σ (i.e., at 95% confidence level). Fe = total Fe.

* See Figure 6 for explanation.

ences are statistically significant throughout all growth stages. The compositional polarity is more pronounced at the outer margin than at the inner margin of the rims grown during stages I and III; the rim of stage II, though, exhibits the opposite relationship (see Table 2). These data demonstrate that the $c+$ pole is systematically richer in Al and $^{X}\square$ but poorer in Ti, Mg, Ca, and Na than the corresponding $c-$ pole in all growth zones, both at their inner and outer margins (Table 2). This relationship cannot be an effect of the geometry of the analyzed section because it was found in all zoned tourmaline crystals from the studied geologic traverse. Because the different zones grew at different metamorphic conditions, it appears that the observed systematic trend in the compositional difference between $c+$ and $c-$ could be a general characteristic of tourmaline, at least for that grown between diagenetic and lower amphibolite-facies conditions. This is supported by the observations of Henry and Dutrow (1992), who reported the same trend for rims grown during low-grade metamorphism (chlorite zone).

TABLE 3. Correlation matrix for major cations in tourmaline rims grown during stage I

	Al	Ti	Fe	Mg	Ca	Na	Si
Al	1						
Ti	−0.941	1					
Fe	0.544	−0.546	1				
Mg	−0.977	0.883	−0.624	1			
Ca	−0.925	0.832	−0.726	0.965	1		
Na	−0.952	0.889	−0.365	0.912	0.826	1	
Si	0.655	−0.682	0.025	−0.640	−0.527	−0.769	1

Note: All data obtained from sample MF1632 (from crystal shown in Fig. 5 and from other crystals).

The characteristic chemical difference between $c+$ and $c-$ of the innermost zone (stage I) is displayed for several components in Figure 6; this figure not only includes the data for the crystal shown in Figure 5 but also those for all other tourmaline crystals from the same sample. Figure 6 indicates that the compositional variation within this zone, and thus the compositional polarity, may be described schematically as

$$[c+] \quad \mathrm{Al} + {}^{X}\square \rightleftharpoons \mathrm{Mg} + \mathrm{Na} + \mathrm{Ti} \quad [c-]. \tag{8}$$

This equation, however, does not fulfill charge-balance requirements. To deduce substitutions that correctly describe the variation, a correlation matrix was calculated for the components of interest; the matrix (Table 3) reveals excellent inverse correlations between Al and all components except Fe and Si, which remain constant at values of 1.41 ± 0.04 and 6.07 ± 0.02 atoms per formula unit, respectively. From Table 3 and crystal-chemical considerations we conclude that the substitutions

$$\mathrm{Na} + \mathrm{Mg} \rightleftharpoons \square + \mathrm{Al} \tag{9}$$

and

$$2\mathrm{Al} \rightleftharpoons \mathrm{Ti} + \mathrm{Mg} \tag{10}$$

best describe the observed compositional polarity of the innermost rim, in agreement with the findings of Henry and Dutrow (1992). The different behaviors of Fe and Mg lead to polar differences in Mg/Fe of the tourmaline rims and thus result in two partition coefficients for the Mg-Fe exchange between tourmaline and coexisting minerals (one each for $c+$ and $c-$; Sperlich 1990; see also Henry and Dutrow 1992).

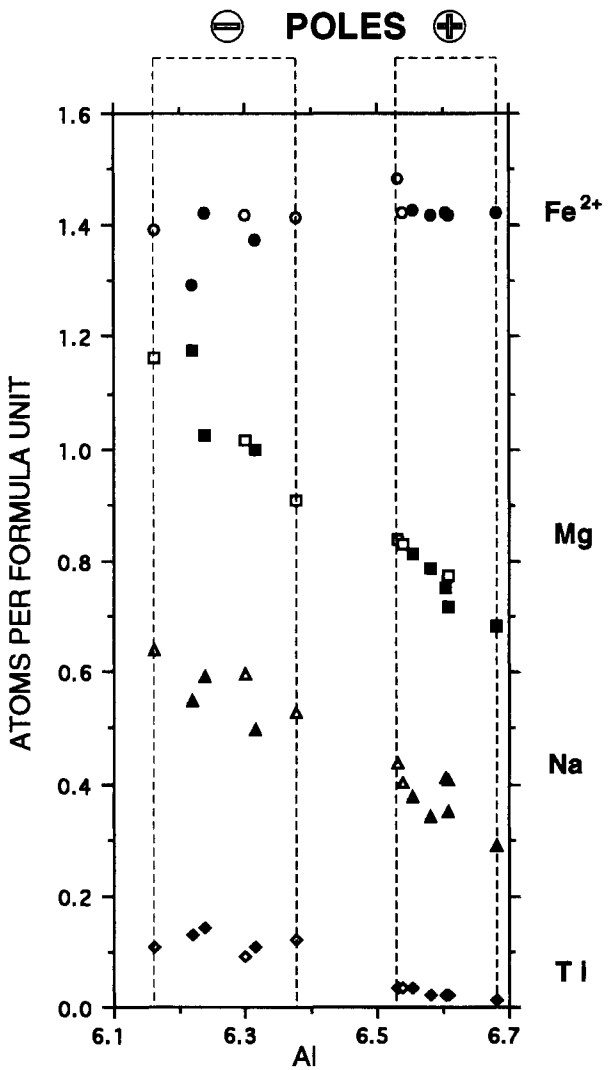

FIGURE 6. Compositional polarity in the innermost rims (stage I). Solid symbols = data of profile shown in Figure 5, open symbols = compositions of innermost rims of other tourmaline crystals from the same sample (sample MF1632). Linear regression data (s = slope, r = correlation coefficient): Mg vs. Al: $s = -0.900 \pm 0.124$, $r = 0.977$; Na vs. Al: $s = -0.593 \pm 0.120$, $r = 0.952$; Ti vs. Al: $s = -0.263 \pm 0.060$, $r = 0.941$; Ca vs. Al: $s = -0.088 \pm 0.022$, $r = 0.925$ (not shown). The value of $Fe^{2+} = 1.3$ (at Al ≈ 6.2) represents an outlier and also accounts for the unusually large Δx_{Fe} listed in Table 2 for the outer margin (marked by asterisk).

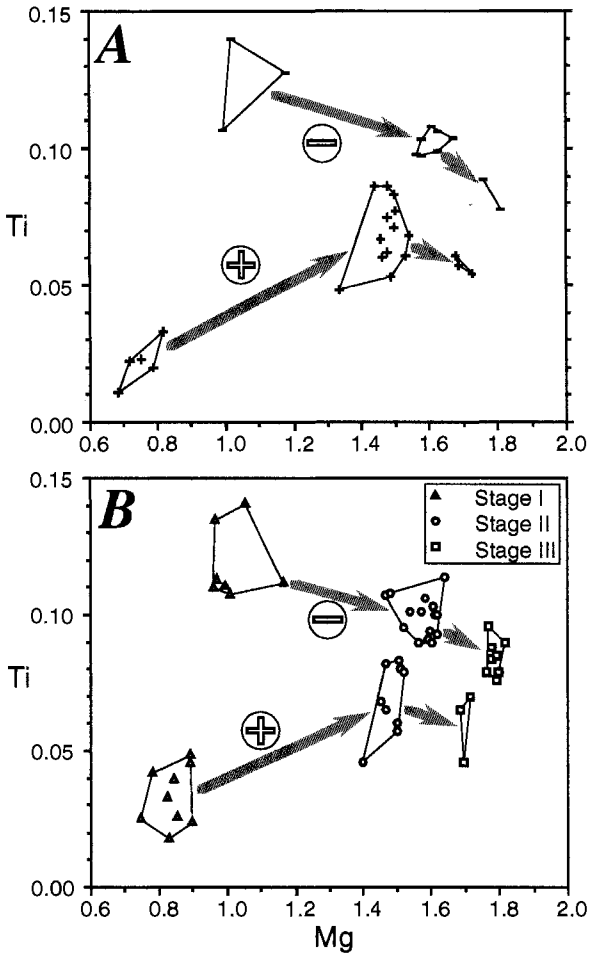

FIGURE 7. Decrease of compositional polarity from internal to external rim zones in tourmaline from amphibolite-facies rocks. The diagrams show the available data for the positive and negative parts of the rims grown during stages I through III. (A) Data of the tourmaline profile shown in Figure 5. (B) Data of other tourmaline crystals in the same sample.

The extent of compositional polarity decreases from stage I to stage III. This is shown in Figure 7 for two components, the concentrations of which converge toward the external tourmaline rims. Convergence of the Ti content, thus, may indeed lead to the disappearance of the distinct color difference between $c+$ and $c-$ from stage I to stage III (see above). The decreasing extent of compositional polarity is also documented in Table 2, where it can be seen that Δx_i decreases from inner to outer zones; only Ca exhibits a compositional polarity that is more pronounced during the later stages. A comparison of Figures 7A and 7B reveals that, if the polar asymmetry is taken into account, all tourmaline crystals from the chosen sample are nearly identical in composition at each of the three growth stages.

A possible explanation for compositional polarity may be provided by the pronounced piezoelectric property of tourmaline: When tourmaline is exposed to mechanical stress, resulting, e.g., from burial of the host rock during diagenesis or from tectonic processes during metamorphism, opposite electrostatic charges may be generated at the two poles. These charges in turn may influence the incorporation of different cations into the crystal structure, e.g., $c-$ possibly favors the highly charged Ti^{4+} rather than Al^{3+} (Sperlich 1990). Our rocks exhibited ample microstructural evidence for mechanical stress. Most of the tourmaline prisms, for example, showed a shape-preferred orientation parallel to the main schistosity; however, the poles are generally not oriented in the same

TABLE 4. Electron microprobe analyses of tourmaline rims grown during stage I (positive pole; in weight percent)

Sample	MF330	MF311	MF226	MF1750	MF479	MF1721	MF1621	MF1579	MF1632	MF1315	MF925
Stratigraphic unit	Keuper	Keuper	Keuper	Keuper	Keuper	Lias	Lias	Lias	Lias	Lias	Lias
B_2O_3*	10.42	10.55	10.54	10.67	10.47	10.35	10.60	10.75	10.63	10.84	10.73
SiO_2	36.5	37.3	37.1	37.5	37.1	36.6	38.0	37.9	37.7	38.7	38.6
Al_2O_3	29.8	32.0	33.4	33.7	33.2	31.6	33.1	33.9	34.6	34.8	34.0
TiO_2	0.54	0.27	0.21	0.32	0.41	0.76	0.47	0.18	0.18	0.44	<0.09
FeO	6.80	7.06	7.80	7.13	10.1	11.8	8.25	6.44	9.70	7.19	8.53
Fe_2O_3*	3.66	1.09	0.56	1.80	1.79	0.23	0.00	1.02	0.85	0.00	0.53
MnO	<0.05	<0.05	<0.05	<0.05	<0.05	<0.05	<0.05	<0.05	<0.05	<0.05	0.05
MgO	6.36	6.08	4.89	4.88	2.65	3.26	4.86	5.73	2.96	5.05	4.22
CaO	0.04	0.08	0.04	0.04	0.06	0.03	0.07	0.08	0.02	0.1	0.03
Na_2O	2.62	2.36	1.9	1.56	0.95	2.22	1.83	1.84	1.11	1.37	1.3
K_2O	0.07	0.02	0.03	0.02	0.07	0.03	0.01	0.01	<0.01	<0.01	<0.01
F	n.d.	n.d.	n.d.	n.d.	n.d.	n.d.	n.d.	n.d.	n.d.	n.d.	n.d.
H_2O*	3.15	3.18	3.18	3.22	3.16	3.12	3.20	3.24	3.21	3.27	3.24
O = F	0.00	0.00	0.00	0.00	0.00	0.00	0.00	0.00	0.00	0.00	0.00
Total	100.0	100.0	99.7	100.8	100.0	100.0	100.3	101.2	100.9	101.7	101.3
Number of ions on the basis of 15 cations and 31 (O + OH + F)											
Si	6.086	6.147	6.124	6.106	6.163	6.144	6.229	6.130	6.166	6.209	6.263
Al	5.858	6.218	6.502	6.476	6.506	6.249	6.393	6.464	6.660	6.567	6.489
Ti	0.068	0.033	0.026	0.039	0.051	0.096	0.058	0.022	0.022	0.053	0.000
Fe_{tot}	1.408	1.108	1.145	1.192	1.624	1.689	1.132	0.995	1.430	0.964	1.221
Mn	0.000	0.000	0.000	0.000	0.000	0.000	0.000	0.007	0.000	0.000	0.007
Mg	1.581	1.494	1.203	1.186	0.656	0.822	1.189	1.381	0.722	1.207	1.020
Ca	0.007	0.014	0.007	0.007	0.011	0.005	0.012	0.014	0.004	0.017	0.005
Na	0.847	0.754	0.608	0.493	0.306	0.723	0.582	0.577	0.352	0.426	0.408
K	0.015	0.004	0.006	0.004	0.015	0.006	0.002	0.002	0.000	0.000	0.000
$B_{assumed}$	3.000	3.000	3.000	3.000	3.000	3.000	3.000	3.000	3.000	3.000	3.000
F	0.000	0.000	0.000	0.000	0.000	0.000	0.000	0.000	0.000	0.000	0.000
OH*	3.500	3.500	3.500	3.500	3.500	3.500	3.500	3.500	3.500	3.500	3.500
O*	27.500	27.500	27.500	27.500	27.500	27.500	27.500	27.500	27.500	27.500	27.500
X-site total	0.869	0.772	0.621	0.504	0.331	0.735	0.596	0.593	0.355	0.443	0.414
X-site vacancies	0.131	0.228	0.379	0.496	0.669	0.265	0.404	0.407	0.645	0.557	0.586
Fe^{2+}*	0.949	0.973	1.076	0.971	1.400	1.659	1.132	0.871	1.326	0.964	1.156
Fe^{3+}*	0.459	0.135	0.069	0.221	0.224	0.030	0.000	0.125	0.105	0.000	0.065
Fe^{3+}/Fe^{2+}	0.48	0.14	0.06	0.23	0.16	0.02	0.00	0.14	0.08	0.00	0.06
$Mg/(Mg + Fe^{2+})$	0.62	0.61	0.53	0.55	0.32	0.33	0.50	0.61	0.35	0.54	0.47
Ca/(Ca + Na)	0.01	0.02	0.01	0.01	0.03	0.01	0.02	0.02	0.01	0.04	0.01

Note: Analyses arranged in order of increasing X-site vacancies within both rock units; n.d. = not determined.
* Calculated according to Grice and Ercit (1993).

direction within a particular thin section. A second explanation for the origin of compositional polarity is offered by Henry and Dutrow (1992), who noted that this polarity may be due to differences in surface energies that could result from the hemimorphism. At this stage, we are unable to explain the causes of compositional polarity.

EVOLUTION OF ZONING DURING METAMORPHISM

In the following discussion, we focus on the compositional evolution of zoning during progressive metamorphism. Most data were obtained from chemical profiles across large longitudinal sections; these data were compared with and complemented by data from cross sections and small grains without cores. Because corresponding compositions of different tourmaline crystals show very little variation within one sample (see above), we determined average compositional trends for each of the 17 studied samples and plotted them separately in the following figures. These trends, therefore, include data for all tourmaline crystals in a particular sample, and they were obtained by using the average compositions of the inner and outer margins of individual rims. The average composition x was calculated as $x = \frac{1}{2}[\Sigma\, x(c+)/m + \Sigma\, x(c-)/n]$. This calculation takes into account that the number of analyses available for the bigger, $c+$ part of each rim (m) is larger than that of the smaller, $c-$ part (n).

A complete data set for tourmaline and coexisting minerals is given by Sperlich (1990). Representative analyses of stage-I rims are given in Table 4, where only data from $c+$ are listed to avoid the effect of compositional polarity. Because of the refractory behavior of tourmaline, the composition of the innermost rims in amphibolite-facies rocks is very similar to that of the rims found in rocks that were subjected to diagenetic or low-grade metamorphic conditions. Regardless of the host-rock composition, all analyses of stage-I tourmaline are characterized by very low CaO contents ($\leq$0.23 wt%). In contrast, Na_2O exhibits wide variation (cf. Table 4, Fig. 6), implying a concomitant variation in $^{X}\square$. Similarly, the Al and Ti contents as well as the ratio $Mg/(Mg + Fe^{2+})$ scatter significantly. Moreover, the rims of stage I vary widely with respect to their Fe^{3+} contents, as calculated according to the normalization procedure of Grice and Ercit (1993). However, the normalization revealed that, in general, only tourmaline from the Keuper redbeds contains significant amounts of Fe^{3+} (cf. Fe^{3+}/Fe^{2+} in Tables 4 and 5).

TABLE 5. Electron microprobe analyses of rims (positive pole; in weight percent) of two zoned tourmaline crystals from the Lukmanier area

	MF160					MF216					
Distance (μm)	3	16	31	41	52	10	150	190	210	230	250
Rim type	stage I	stage I	stage II	stage II	stage III	stage I	stage I	stage II	stage II	stage III	stage III
B_2O_3*	10.77	10.68	10.93	10.89	10.77	10.50	10.46	10.51	10.64	10.61	10.51
SiO_2	38.3	37.9	38.9	38.5	37.5	36.6	36.6	36.8	37.0	36.9	36.2
Al_2O_3	35.0	35.1	35.3	34.2	33.6	31.0	31.0	30.6	31.4	32.4	32.0
TiO_2	0.15	0.18	0.29	0.35	0.46	0.55	0.21	0.33	0.31	0.64	0.40
FeO	8.61	8.84	4.49	4.34	5.57	5.43	4.58	4.42	4.18	4.76	3.78
Fe_2O_3	0.70	0.32	0.00	0.00	0.15	3.17	2.47	2.21	2.42	0.25	1.61
MnO	<0.05	<0.05	0.05	<0.05	<0.05	0.09	<0.05	<0.05	<0.05	<0.05	<0.05
MgO	3.72	3.43	6.60	7.61	7.23	6.74	7.48	8.15	8.25	7.90	8.15
CaO	0.04	0.03	0.11	0.39	0.75	0.07	0.14	0.54	0.93	1.12	1.24
Na_2O	1.10	1.03	1.36	1.86	1.71	2.40	2.54	2.50	2.12	1.75	1.72
K_2O	0.02	0.02	0.02	0.02	0.05	0.02	0.02	<0.01	0.03	0.03	0.01
F	<0.1	<0.1	0.12	0.37	0.31	n.d.	n.d.	n.d.	n.d.	n.d.	n.d.
H_2O*	3.25	3.22	3.27	3.20	3.18	3.17	3.16	3.17	3.21	3.20	3.17
O = F	0.00	0.00	0.05	0.16	0.13	0.00	0.00	0.00	0.00	0.00	0.00
Total	101.7	100.8	101.4	101.5	101.1	99.8	98.7	99.3	100.5	99.6	98.8
Number of ions on the basis of 15 cations and 31 (O + OH + F)											
Si	6.177	6.174	6.179	6.141	6.051	6.059	6.091	6.087	6.038	6.047	5.989
Al	6.663	6.729	6.619	6.428	6.385	6.051	6.083	5.975	6.046	6.263	6.230
Ti	0.018	0.022	0.035	0.042	0.056	0.068	0.026	0.041	0.038	0.079	0.050
Fe_{tot}	1.247	1.243	0.597	0.579	0.769	1.146	0.945	0.887	0.869	0.682	0.723
Mn	0.000	0.000	0.007	0.000	0.000	0.013	0.000	0.000	0.000	0.000	0.000
Mg	0.895	0.832	1.564	1.810	1.739	1.663	1.854	2.010	2.009	1.929	2.009
Ca	0.007	0.005	0.019	0.067	0.130	0.012	0.025	0.096	0.163	0.197	0.220
Na	0.344	0.325	0.419	0.575	0.535	0.770	0.819	0.802	0.671	0.556	0.551
K	0.004	0.004	0.004	0.004	0.010	0.004	0.004	0.000	0.006	0.006	0.002
$B_{assumed}$	3.000	3.000	3.000	3.000	3.000	3.000	3.000	3.000	3.000	3.000	3.000
F	0.000	0.000	0.060	0.187	0.158	0.000	0.000	0.000	0.000	0.000	0.000
OH*	3.500	3.500	3.470	3.407	3.421	3.500	3.500	3.500	3.500	3.500	3.500
O*	27.500	27.500	27.470	27.407	27.421	27.500	27.500	27.500	27.500	27.500	27.500
X-site total	0.355	0.334	0.442	0.646	0.675	0.787	0.848	0.897	0.840	0.758	0.773
X-site vacancies	0.645	0.666	0.558	0.354	0.325	0.213	0.152	0.103	0.160	0.242	0.227
Fe^{2+}*	1.162	1.203	0.597	0.579	0.751	0.751	0.636	0.612	0.571	0.652	0.522
Fe^{3+}*	0.084	0.039	0.000	0.000	0.018	0.395	0.309	0.275	0.298	0.030	0.201
Fe^{3+}/Fe^{2+}	0.07	0.03	0.00	0.00	0.02	0.53	0.49	0.45	0.52	0.05	0.38
$Mg/(Mg + Fe^{2+})$	0.44	0.41	0.71	0.73	0.70	0.69	0.74	0.77	0.78	0.75	0.79
Ca/(Ca + Na)	0.02	0.02	0.04	0.10	0.20	0.02	0.03	0.11	0.20	0.26	0.29

Note: Sample MF160 is a Lias black shale (lower amphibolite facies), sample MF216 is a Keuper redbed (lower amphibolite facies). The indicated distance is measured from the detrital core toward the positive end of the crystal; n.d. = not determined.

* Calculated according to Grice and Ercit (1993).

Two examples of the compositional variation in tourmaline from the upper greenschist and lower amphibolite facies are given in Table 5. The data represent single-spot analyses of each of the three zones. Chemically, the discontinuous boundary between the rims of stages I and II is reflected in particular by an increase in Ca and Mg and by a decrease in total Fe. Within the rims of stage II the values for both Ca and $Mg/(Mg + Fe^{2+})$ further increase toward the outer margin. The data further demonstrate that compositional differences between the two grains of tourmaline are pronounced in the innermost zones but less marked in the most external rims, indicating that the composition of tourmaline tends to converge with respect to several components at higher metamorphic grade. This general compositional convergence during prograde metamorphism from diagenetic to amphibolite-facies conditions is displayed in Figures 8 through 11.

Figure 8 shows the prograde compositional evolution of tourmaline in the vector triangle defined by alkali-free tourmaline, dravite-schorl, and uvite (cf. Fig. 1A). All low-grade rims plot close to the tieline between dravite-schorl and alkali-free tourmaline because of the very low Ca contents and the wide variation in Na (cf. Tables 4 and 5); the variability of the low-grade rims with respect to $^{X}\square$ appears to be slightly larger in the Keuper redbeds than in the Lias black shales. The compositional discontinuity at the beginning of the second growth zone (stage II) leads to the first significant increase in Ca. During stage II, the Ca content continuously increases outward. A similar trend was observed in the rims grown under amphibolite-facies conditions (stage III); the Ca content, however, does not increase in all samples during this stage (e.g., tourmaline from the Keuper). The convergence of tourmaline compositions with respect to $^{X}\square$ during progressive metamorphism is achieved by distinct trends. The character of the compositional trends appears to depend on the initial alkali deficiency: Tourmaline with initial X-site vacancies of 0.4–0.6 generally displays a trend parallel to $Ca(M_x)_2\square_{-1}Al_{-2}$ (cf. Fig. 1A), whereas tourmaline starting with 0.1–0.2 $^{X}\square$ more closely follows $\square CaNa_{-2}$.

The configuration of Figure 1B is used in Figure 9 to

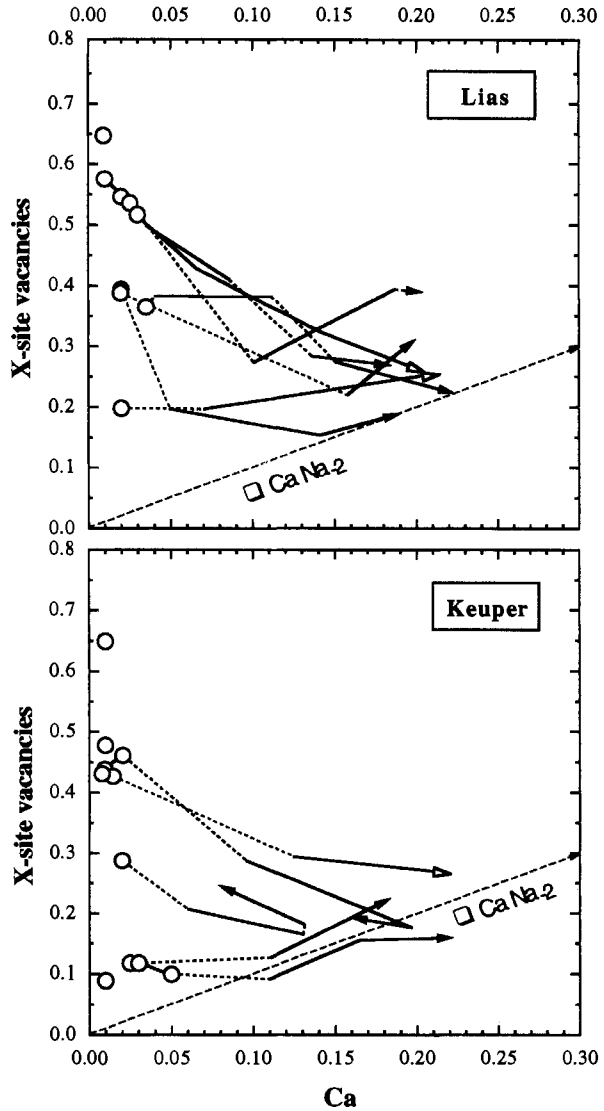

FIGURE 8. Prograde compositional evolution of tourmaline, plotted on the basal face of the vector prism (see Fig. 1A). Note the convergence of tourmaline composition with increasing metamorphic grade. Open symbols = stage-I rims, dashed lines = discontinuous zoning, solid lines = continuous zoning, open arrows = tourmaline occurring in greenschist-facies rocks, and solid arrows = tourmaline occurring in amphibolite-facies rocks.

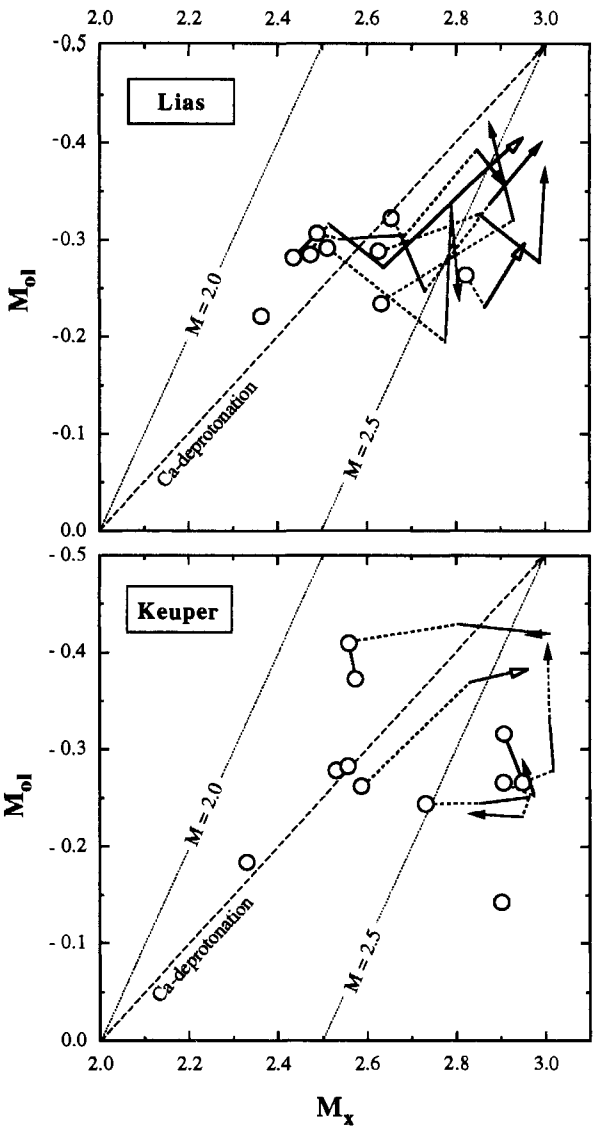

FIGURE 9. Prograde compositional evolution of tourmaline, plotted on the back face of the vector prism (see Fig. 1B). The Ca-deprotonation vector of Henry and Dutrow (1990) is given for reference. Same symbols as in Figure 8.

display the compositional evolution with respect to M_x and M_{ol}. In general, the individual trends show an increase in M, which takes place at the expense of Al (cf. Fig. 1B); only some of the initially M_x-rich samples exhibit reversed zoning. The trends shown in Figure 9 reveal that the compositional difference between individual samples generally decreases with increasing metamorphic grade; this is particularly evident for the Keuper samples. The general compositional convergence is again achieved by distinct trends that, for most samples, exhibit a pronounced change in direction at the transition between stages II and III. For some Keuper samples, the chemical evolution takes place at almost constant M_{ol} values, i.e., nearly parallel to $Ca(M_x)_2\square_{-1}Al_{-2}$, whereas for others there are significant changes in M_{ol} toward the outer rims. A particularly sharp increase in the olenite content, for example, was observed for tourmaline compositions characterized by $M_x \approx 3.0$, a value that was reached during stage II and defines the upper limit of M_x in our samples. One Keuper sample reached $M_x \approx 3.0$ at $M_{ol} = -0.4$ at the end of stage II, but its olenite content did not further increase during subsequent growth. These observations, thus, indicate that the composition of tourmaline tends to converge toward $M_x \approx 3$ and $M_{ol} \approx -0.4$ during the final stages of tourmaline growth, a trend that was observed for both lithologic units. In summary, Figure 9

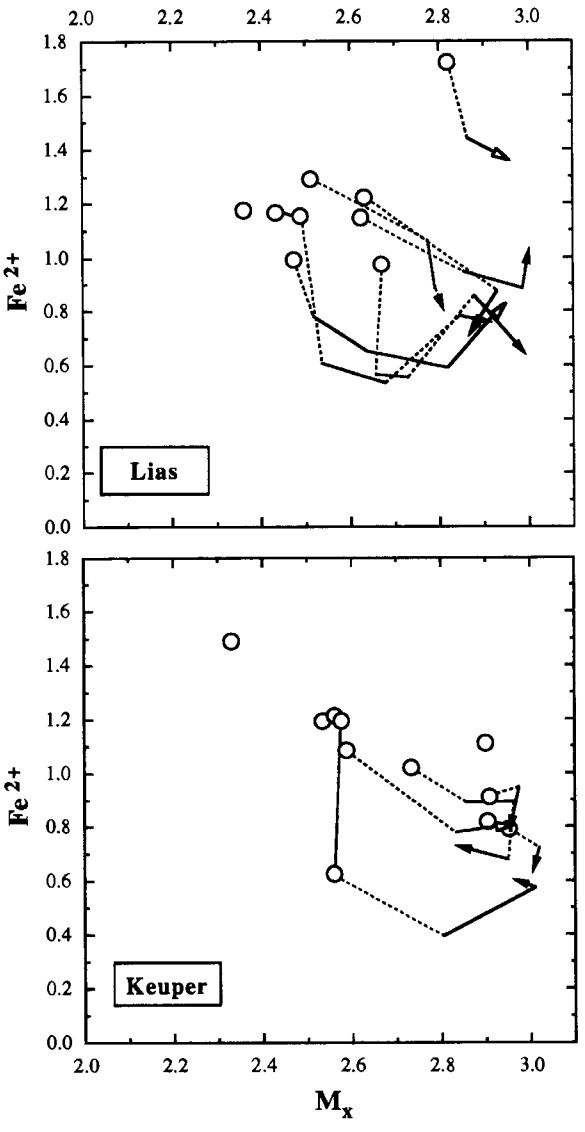

FIGURE 10. Prograde compositional evolution of tourmaline, plotted on the back face of the vector prism (see Fig. 1C). Same symbols as in Figure 8.

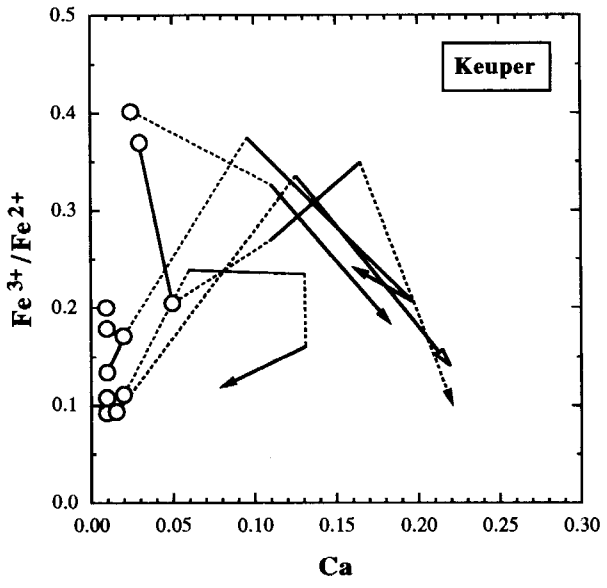

FIGURE 11. Prograde compositional evolution of tourmaline from the Keuper redbeds. Same symbols as in Figure 8.

clearly shows that the Ca-deprotonation vector of Henry and Dutrow (1990) can be used merely as an overall approximation in describing the complex compositional evolution of the studied tourmaline; only three Lias samples exhibit for their continuously zoned external rims a trend that is parallel to the Ca-deprotonation vector.

The contribution of the $FeMg_{-1}$ vector to the evolution of tourmaline is displayed in Figure 10, which represents the back face of the vector prism (cf. Fig. 1C). Figure 10 shows that the discontinuous transition between stages I and II is marked by a pronounced decrease in Fe^{2+} for almost all studied crystals. Moreover, it can be seen that the final Fe^{2+} content of tourmaline is always smaller than the corresponding initial content. This overall decrease in Fe^{2+} with increasing metamorphic grade was observed in tourmaline from both rock types. The trend is not continuous, however, and reaches a minimum for some samples during intermediate growth stages. The data further reveal that Fe^{2+} is involved in both substitutions displayed in Figure 10, i.e., $FeMg_{-1}$ and $Ca(M_x)_2\square_{-1}Al_{-2}$; only occasionally, the variation in Fe^{2+} can be described solely by the simple $FeMg_{-1}$ exchange (nearly vertical trends in Fig. 10).

The prograde evolution of tourmaline with respect to its Fe^{3+} content is discussed for only the Keuper samples because tourmaline occurring in the Lias black shales usually contains negligible amounts of Fe^{3+}. The trends for Fe^{3+}/Fe^{2+} with increasing metamorphic grade, represented by increasing Ca (see Fig. 8), are depicted in Figure 11, which shows that the rims grown during stage I do not exhibit a uniform distribution of Fe between Fe^{3+} and Fe^{2+}. The distinct chemical discontinuity between the rims of stages I and II (see Figs. 8–10) is also conspicuous in this diagram and is characterized by a pronounced increase in Fe^{3+}/Fe^{2+}. Only one sample does not follow the described trend, probably because its innermost rim contains the highest proportion of Fe^{3+}; again, this suggests that the initial composition of tourmaline is an important factor in determining the chemical evolution during later stages of metamorphism. Figure 11 further demonstrates that the Fe^{3+}/Fe^{2+} values in tourmaline reached a maximum during stage II, i.e., under greenschist-facies conditions, and then generally decreased at the onset of and during stage III. The latter is consistent with the observations of Frey (1969), who reported that the amphibolite-facies rocks from the Lukmanier area are less oxidized than the equivalent lower-grade rocks farther north.

Although the compositional evolution of tourmaline

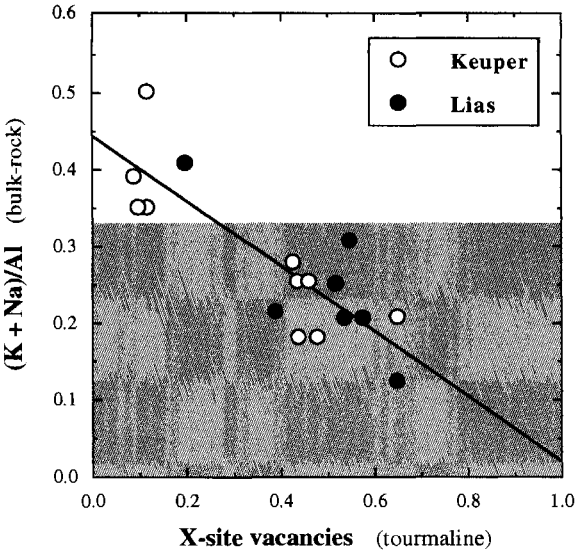

FIGURE 12. Correlation of compositions of stage-I rims (average values) with composition of the host rock (correlation coefficient $r = 0.838$). Note that of the samples shown in Figure 8 only those are plotted for which bulk-rock data are available. For samples with compositional zoning within stage-I rims, two dots are plotted at the same bulk-rock composition. Shaded area represents clay- and muscovite-rich host rocks.

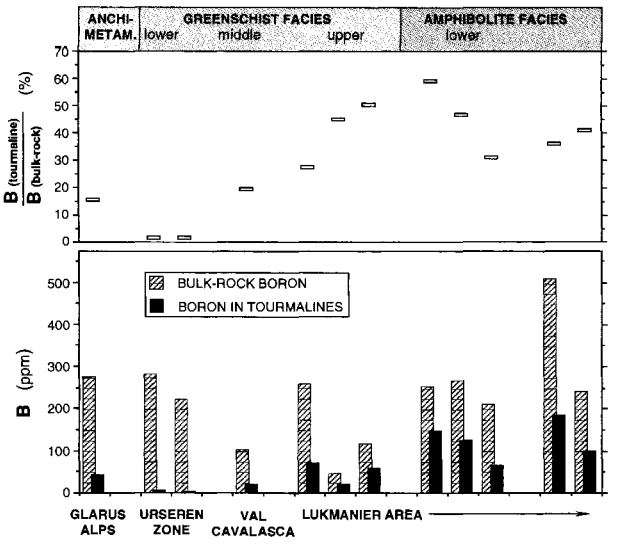

FIGURE 13. Variation of B in host rock and in tourmaline rims, displayed in order of increasing metamorphic grade. Bulk-rock B content analyzed by inductively coupled plasma-emission spectroscopy (after pyrohydrolysis of rock powders; Luecke 1984); B contained in tourmaline calculated from the modal abundance of stoichiometric tourmaline (theoretical content of 3.0 B per formula unit).

during prograde metamorphism is usually distinct for individual samples, some general similarities can be recognized. The scattering of the data is largest in the innermost rims (stage I) and decreases during later stages. Moreover, the most pronounced discontinuity is found between stages I and II, and the final composition of tourmaline from greenschist-facies rocks is in general very similar to that of tourmaline from amphibolite-facies rocks. These observations document the convergence of tourmaline compositions at higher metamorphic grades. The overall increase in Mg at the expense of Fe^{2+} during the progressive metamorphism (cf. Table 5, Fig. 7) parallels the progressive enrichment of Mg in other ferromagnesian silicates; similar systematic Fe-Mg zoning in tourmaline was also reported by, e.g., Grew and Sandiford (1984), Henry and Guidotti (1985), and Henry and Dutrow (1992). In almost all tourmaline crystals, Ca increases from internal to external rims. Because Na decreases simultaneously, the ratio Ca/(Ca + Na) increases outward (cf. Table 5; see also Grew and Sandiford 1984; Madore and Perreault 1987). These observations suggest that increasing values of Ca/(Ca + Na) and Mg/(Mg + Fe^{2+}) in zoned tourmaline may generally reflect increasing metamorphic grade. From Figures 8–10 it is further evident that the compositional trends of the Keuper redbeds are very similar to those of the Lias black shales. The only significant difference is observed for the oxidation state of Fe. The very low or lacking Fe^{3+} contents of tourmaline from the Lias samples are probably directly related to the presence of some organic material throughout the whole traverse.

TOURMALINE AND ITS HOST-ROCK COMPOSITION

If all stage-I rims of tourmaline grew under similar P-T conditions, the large variability of their chemical composition may be the result of differences in the host-rock compositions. This suggestion is supported by a fairly good negative correlation between $^{X}\square$ in tourmaline and the ratio (K + Na)/Al in the bulk rock (Fig. 12). In low-grade clastic sediments, detrital alkali feldspars, micas, and clay minerals carry most of the alkali elements. Because the presence of other Al-bearing minerals would lower the whole-rock (K + Na)/Al ratio, the bulk value can be used as an estimate of the relative proportions of the minerals present in the original sedimentary rock: A rock containing illite as sole alkali-bearing mineral would have a (K + Na)/Al value of 0.2–0.3, whereas a rock containing only muscovite would have a value of 0.33; these values would be increased by the presence of alkali feldspars. Values above 0.33, thus, point to the presence of significant amounts of detrital alkali feldspars. As revealed by Figure 12, sediments with significant amounts of detrital alkali feldspars, and thus high (K + Na)/Al ratios, favor the growth during stage I of tourmaline crystals that have almost complete X-site occupancies (i.e., rich in Na) and concomitantly are relatively poor in Al. A similar conclusion was also reached by Werding and Schreyer (1984). Conversely, it appears that all stage-I

rims with $^{X}\square \leq 0.26$ are associated with considerable alkali feldspar concentrations in the sedimentary protolith. Our observations indicate that the host-rock composition significantly affected the initial tourmaline composition and, in turn, the chemical evolution during diagenesis and low-grade metamorphism.

The observed extensive growth of tourmaline during prograde metamorphism suggests that (1) tourmaline grew at the expense of other B-bearing minerals or (2) B was introduced to the rock units from external sources. The volumetrically large rims did not grow at the expense of detrital tourmaline grains, as demonstrated by the preservation of the detrital cores up to amphibolite-facies conditions.

Figure 13 displays the relation between the bulk-rock B contents, the amount of B fixed in tourmaline, and metamorphic grade. Average whole-rock B concentrations are approximately 200 ppm and show no systematic trend with increasing metamorphic grade. The amount of B fixed in tourmaline increases significantly at the transition from middle to upper greenschist-facies conditions because of the extensive growth of tourmaline during stage II (cf. Fig. 5). At this transition and at higher grades, however, 40–65% of the bulk-rock B is still accommodated in minerals other than tourmaline (Fig. 13). These observations suggest that B influx from external sources can be ruled out, in agreement with the interpretation of Frey (1969, p. 133); therefore, the B required for the growth of tourmaline during metamorphism was derived from other B-bearing minerals in the original sedimentary rocks. This conclusion is supported by the presence of compositional discontinuities between the rims indicating that B was sporadically available. Intermittent availability is best explained if B was released during the breakdown of other B-bearing minerals as a consequence of metamorphic reactions.

Pelitic sediments usually contain significantly more B than quartz- or carbonate-rich sedimentary rocks because clay minerals, particularly illite, may concentrate B (Harder 1961; Stubican and Roy 1962; Brockamp 1973). With increasing metamorphic grade, B is released by recrystallization or breakdown of illite and muscovite and becomes available for tourmaline growth (Weaver and Broekstra 1984). Therefore, in regional metamorphic terrains illite represents a very important B source (Landergren 1945; Harder 1961; Reynolds 1965). The results presented here, thus, suggest that the B necessary to form the large tourmaline overgrowths was derived in the early stages from the continuous transformation of illite into muscovite (anchimetamorphic to greenschist-facies conditions; Hunziker et al. 1986) and, in the later stages, from the breakdown of muscovite (taking place at upper greenschist- and lower amphibolite-facies conditions).

Acknowledgments

This paper summarizes the Ph.D. thesis of R.S. (completed in 1990), who visited D.J. Henry in 1989 to discuss the main results. The manuscript benefited from careful reviews by E.S. Grew, D.J. Henry, and T.C. Labotka, to whom we express our sincere gratitude. We appreciate constructive discussions with J. Abrecht and are grateful to M. Dalla Torre for preparing some of the figures. We also thank the Schweizerischer Nationalfonds for financial support (grant 20.5196.86 to M.F.; grants 8220–037190 and 2124–042200.94 to R.G.).

References cited

Alty, S.W. (1933) Some properties of authigenic tourmaline from lower Devonian sediments. American Mineralogist, 18, 351–355.

Awashti, N. (1961) Authigenic tourmaline and zircon in the Vindhyan formations of Sone Valley, Mizapur District, Uttar Pradesh, India. Journal of Sedimentary Petrology, 31, 482–484.

Barton, R., Jr. (1969) Refinement of the crystal structure of buergerite and absolute orientation of tourmalines. Acta Crystallographica, B25, 1524–1532.

Brockamp, O. (1973) Borfixierung in authigenen und detritischen Tonen. Geochimica et Cosmochimica Acta, 37, 1339–1351.

Burt, D.M. (1989) Vector representation of tourmaline compositions. American Mineralogist, 74, 826–839.

Deer, W.A., Howie, R.A., and Zussman, J. (1992) An introduction to the rock-forming minerals (2nd edition), p. 130–137. Longman, Essex, U.K.

Dietrich, R.V. (1985) The tourmaline group, 300 p. Van Nostrand Reinhold, New York.

Dutrow, B.L., Holdaway, M.J., and Hinton, R.W. (1986) Lithium in staurolite and its petrologic significance. Contributions to Mineralogy and Petrology, 94, 496–506.

Dutrow, B.L., and Henry, D.J. (1994) Crystal chemistry of tourmaline: A guide to metamorphic evolution of metapelites. International Mineralogical Association, 16th General Meeting, Pisa (abs. vol.), 108.

Engi, M., Todd, C.S., and Schmatz, D. (1995) Tertiary metamorphic conditions in the eastern Lepontine Alps. Schweizerische Mineralogische und Petrographische Mitteilungen, 75, 347–369.

Foit, F.F., Jr., and Rosenberg, P.E. (1977) Coupled substitutions in the tourmaline group. Contributions to Mineralogy and Petrology, 62, 109–127.

Fox, J.S. (1975) Three-dimensional isograds from the Lukmanier Pass, Switzerland, and their tectonic significance. Geological Magazine, 112, 547–564.

Frey, M. (1969) Die Metamorphose des Keupers vom Tafeljura bis zum Lukmanier-Gebiet. Beiträge zur Geologischen Karte der Schweiz, Neue Folge, 137 p.

——— (1974) Alpine metamorphism of pelitic and marly rocks of the Central Alps. Schweizerische Mineralogische und Petrographische Mitteilungen, 54, 489–506.

——— (1978) Progressive low-grade metamorphism of a black shale formation, Central Swiss Alps, with special reference to pyrophyllite- and margarite-bearing assemblages. Journal of Petrology, 19, 95–135.

Gieré, R., and Rumble, D. (1994a) History of tourmaline growth in metamorphic schists from the Central Alps. Carnegie Institution of Washington Year Book, 93, 90–91.

——— (1994b) Growth and corrosion of tourmaline during metamorphism of pelitic rocks from the Central Alps. Geological Society of America, Annual Meeting (abs. vol.), A-449.

Grew, E.S., and Sandiford, M. (1984) A staurolite-talc assemblage in tourmaline-phlogopite-chlorite schist from northern Victoria Land, Antarctica, and its petrologic significance. Contributions to Mineralogy and Petrology, 87, 337–350.

Grew, E.S., Chernosky, J.V., Werding, G., Abraham, K., Marquez, N., and Hinthorne, J.R. (1990) Chemistry of kornerupine and associated minerals, a wet chemical, ion microprobe, and X-ray study emphasizing Li, Be, B and F contents. Journal of Petrology, 31(5), 1025–1070.

Grice, J.D., and Robinson, G.W. (1989) Feruvite, a new member of the tourmaline group, and its crystal structure. Canadian Mineralogist, 27, 199–203.

Grice, J.D., and Ercit, T.S. (1993) Ordering of Fe and Mg in the tourmaline crystal structure: The correct formula. Neues Jahrbuch für Mineralogie Abhandlungen, 165(3), 245–266.

Harder, H. (1961) Einbau von Bor in detritische Tonminerale: Experimente zur Erklärung des Borgehaltes toniger Sedimente. Geochimica et Cosmochimica Acta, 21, 284–294.

Henry, D.J., and Guidotti, C.V. (1985) Tourmaline as a petrogenetic indicator mineral: An example from the staurolite-grade metapelites of NW Maine. American Mineralogist, 70, 1–15.

Henry, D.J., and Dutrow, B.L. (1990) Ca substitution in Li-poor aluminous tourmaline. Canadian Mineralogist, 28, 111–124.

——— (1992) Tourmaline in a low grade clastic metasedimentary rock: An example of the petrogenetic potential of tourmaline. Contributions to Mineralogy and Petrology, 112, 203–218.

Hunziker, J.C., Frey, M., Clauer, N., Dallmeyer, R.D., Friedrichsen, H., Flehmig, W., Hochstrasser, K., Roggwiler, P., and Schwander, H. (1986) The evolution of illite to muscovite: Mineralogical and isotopic data from the Glarus Alps, Switzerland. Contributions to Mineralogy and Petrology, 92, 157–180.

Krynine, P.D. (1946) The tourmaline group in sediments. Journal of Geology, 54, 65–87.

Landergren, S. (1945) Contributions to the geochemistry of boron II: The distribution of boron in some Swedish sediments, rocks and iron ores: The boron cycle of the upper lithosphere. Arkiv för Kemi Mineralogi och Geologi, 19A(26), 1–31.

Lowell, G.R., and Vierrether, C.B. (1989) Chemical and optical zoning in tourmaline from northeastern Pará, Brazil. Geological Society of America Abstracts with Programs, 21(6), 43.

Luecke, W. (1984) ICP-AES-Bestimmung sehr kleiner Borgehalte in geologischem Material. In B. Welz, Ed., Fortschritte in der atomspektroskopischen Spurenanalytik, p. 261–266. Chemie, Weinheim, Germany.

Mader, D. (1978) Turmalinauthigenese im Buntsandstein von Oberbettingen (Westeifel). Neues Jahrbuch für Mineralogie Monatshefte, 233–240.

——— (1980) Turmalinauthigenese in Bröckelbänken aus dem oberen Buntsandstein der nördlichen Trierer Bucht (Westeifel). Aufschluss, 31, 249–256.

Madore, C., and Perreault, S. (1987) Behavior of tourmaline in the prograde metamorphism of pelitic schists, Labrador Trough, Kuujjuac, Quebec. Geological Association of Canada Program with Abstracts, 12, 70.

Povondra, P. (1981) The crystal chemistry of tourmalines of the schorl-dravite series. Acta Universitatis Carolinae-Geologica, 3, 223–264.

Reynolds, R.C., Jr. (1965) Geochemical behavior of boron during the metamorphism of carbonate rocks. Geochimica et Cosmochimica Acta, 29, 1101–1114.

Schreyer, W., Abraham, K., and Behr, H.J. (1975) Sapphirine and associated minerals from the kornerupine rock of Waldheim, Saxony. Neues Jahrbuch für Mineralogie Abhandlungen, 126, 1–27.

Slack, J.F., and Coad, P.R. (1989) Multiple hydrothermal and metamorphic events in the Kidd Creek vulcanogenic massive sulfide deposit, Timmins, Ontario: Evidence from tourmalines and chlorites. Canadian Journal of Earth Sciences, 26, 694–715.

Smith, D.C. (1971) A tourmaline-bearing eclogite from Sunmore, Norway. Norsk Geologisk Tidsskrift, 51, 141–147.

Sperlich, R. (1990) Zoning and crystal chemistry of tourmalines in prograde metamorphic sequences of the Central Alps. Ph.D. thesis, University of Basel, Switzerland.

Stubican, V., and Roy, R. (1962) Boron substitution in synthetic micas and clays. American Mineralogist, 47, 1166–1173.

Thakur, V.C. (1972) Computation of the values of the finite strains in the Molare region, Ticino, Switzerland, using stretched tourmaline crystals. Geological Magazine, 109(5), 445–450.

Thompson, J.B., Jr. (1982) Composition space: An algebraic and geometric approach. In Mineralogical Society of America Reviews in Mineralogy, 10, 1–31.

Weaver, C.E., and Broekstra, B.R. (1984) Illite-mica. In C.E. Weaver et al., Eds., Shale slate metamorphism in southern Appalachians, p. 67–199. Elsevier, Amsterdam.

Werding, G., and Schreyer, W. (1984) Alkali-free tourmaline in the system MgO-Al_2O_3-B_2O_3-SiO_2-H_2O. Geochimica et Cosmochimica Acta, 48, 1331–1344.

Manuscript received August 21, 1995
Manuscript accepted May 10, 1996